Inorganic Chemistry

pubs.acs.org/IC Article

Atomic-Scale Tuning of Tsai-Type Clusters in RE−Au−Si Systems (RE = Gd, Tb, Ho)

Girma Gebresenbut,* Takayuki Shiino, Daniel Eklöf, Deep Chandra Joshi, Fernand Denoel, Roland Mathieu, Ulrich Häussermann, and Cesar Pay Gómez*

Cite This: *Inorg. Chem.* 2020, 59, 9152−9162 Read Online

ACCESS | Metrics & More | Article Recommendations | Supporting Information

ABSTRACT: Tsai-type quasicrystals and approximants are distinguished by a cluster unit made up of four concentric polyhedral shells that surround a tetrahedron at the center. Here we show that for Tsai-type 1/1 approximants in the RE−Au−Si systems (RE = Gd, Tb, Ho) the central tetrahedron of the Tsai clusters can be systematically replaced by a single RE atom. The modified cluster is herein termed a "pseudo-Tsai cluster" and represents, in contrast to the conventional Tsai cluster, a structural motif without internal symmetry breaking. For each system, single-phase samples of both pseudo-Tsai and Tsai-type 1/1 approximants were independently prepared as millimeter-sized, faceted, single crystals using the self-flux synthesis method. The full replacement of tetrahedral moieties by RE atoms in the pseudo-Tsai 1/1 approximants was ascertained by a combination of single-crystal and powder diffraction studies, as well as energy dispersive X-ray spectroscopy (EDX) analyses with a scanning electron microscope (SEM). Differential scanning calorimetry (DSC) studies revealed distinctly higher decomposition temperatures, by 5−35 K, for the pseudo-Tsai phases. Furthermore, the magnetic properties of pseudo-Tsai phases are profoundly and consistently different from the Tsai counterparts. The onset temperatures of magnetic ordering (T_{mag}) are lowered in the pseudo-Tsai phases by ∼30% from 24 to 17 K, 11.5 to 8 K, and 5 to 3.5 K in the Gd−Au−Si, Tb−Au−Si, and Ho−Au−Si systems, respectively. In addition, the Tb−Au−Si and Ho−Au−Si systems exhibit some qualitative changes in their magnetic ordering, indicating decisive changes in the magnetic state/structure by a moment-bearing atom at the cluster center.

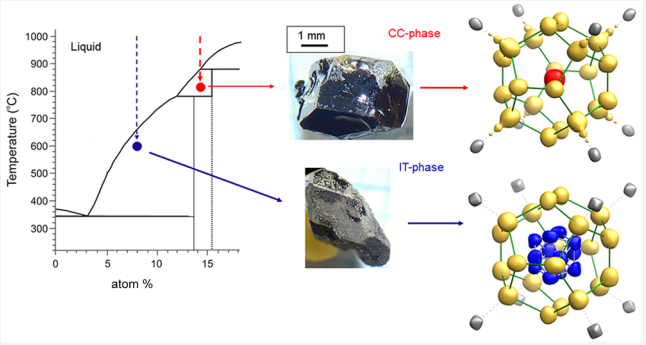

I. INTRODUCTION

The discovery of quasicrystals (QCs) in the early 1980s has provided a new perspective for realizing long-range positional order without imposing periodicity in three dimensions.[1] The atomic arrangement of a QC can be described as a projection of a periodic lattice in higher dimensions (hyperspace).[2] According to this description, the nonperiodic structures of QCs in 3D are irrational projections from their periodic structures in hyperspace. The method benefits from a prior knowledge of local atomic arrangements (atomic clusters) in the QCs to fully model their structures.[3] Approximants of quasicrystals (ACs) are conventional crystals (3D periodic) with atomic clusters and chemical compositions similar to those of their related QCs.[4] ACs play a pivotal role by providing local structural information needed to determine the structures of QCs. Unlike the case for QCs, AC structures can be determined using standard crystallographic techniques.

The largest and most investigated group of QCs and ACs is the Tsai-type group. It is distinguished by its specific constituent atomic cluster type.[5] A conventional Tsai cluster is made up of four concentric polyhedral shells around a central tetrahedron which usually exhibits positional disorder under ambient conditions. The first shell is a dodecahedron, which is followed by a RE icosahedron. The third and fourth shells are an icosidodecahedron and a rhombic triacontahedron, respectively.[3] Figure 1 shows the Tsai cluster of the 1/1 AC in the Gd−Au−Si system (space group $Im\bar{3}$). There are subtle but important structural variations between the parent Tsai-type 1/1 AC, $YbCd_6$, and corresponding ACs in ternary systems. The prototype compound is binary, and Yb and Cd atoms reside unambiguously on their preferred atomic shells: Yb is only found in the icosahedral shell, whereas Cd forms the remaining shells as well as the central tetrahedron. Under ambient conditions this tetrahedron is orientationally disordered: crystallographically the four vertices distribute over 12

Received: April 7, 2020
Published: June 11, 2020

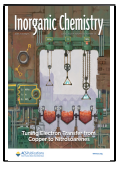

https://dx.doi.org/10.1021/acs.inorgchem.0c01023
Inorg. Chem. 2020, 59, 9152−9162

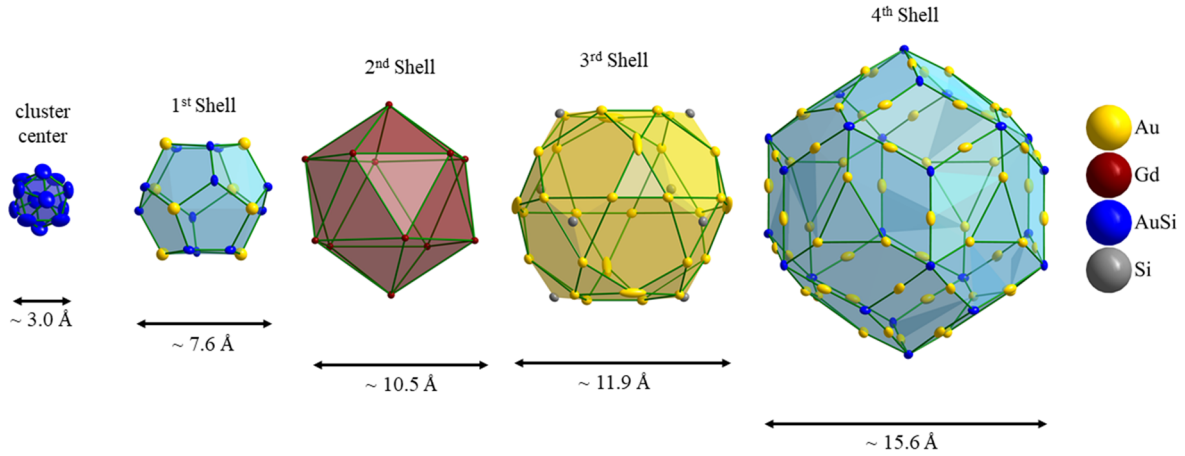

Figure 1. A Tsai-type cluster unit: arranged from left to right we see a disordered tetrahedron, dodecahedron, RE-icosahedron, icosidodecahedron, and rhombic-triacontahedron, respectively. The polyhedra were plotted using the refined structure model of a Gd−Au−Si standard Tsai-type 1/1 AC (space group $Im\bar{3}$). The cluster units are centered at the lattice points (Wyckoff position 2a), forming a *bcc* packing of interpenetrating triacontahedral clusters. Atomic positions have been displayed by thermal ellipsoids at the 70% probability level. The polyhedra have been proportionally scaled with respect to each other.

Table 1. Synthesis Conditions Used to Prepare Tsai and Pseudo-Tsai 1/1 ACs[a]

sample	starting nominal composition	reactants	starting total wt (g)	cooling rate (°C/h)	centrifuging temp (°C)
GAS(IT)	$Gd_{11}(Au_{0.79}Si_{0.21})_{89}$	Gd + $Au_{79}Si_{21}$	~2	~0.8	~600
GAS(CC)	$Gd_{14}(Au_{0.79}Si_{0.21})_{86}$	Gd + $Au_{79}Si_{21}$	~3.5	~1	~830
TAS(IT)	$Tb_5(Au_{0.79}Si_{0.21})_{95}$	Tb + $Au_{79}Si_{21}$	~5	~2	~400
TAS(CC)	$Tb_{15}(Au_{0.79}Si_{0.21})_{85}$	Tb + $Au_{79}Si_{21}$	~1.5	~1	~836
HAS(IT)	$Ho_8(Au_{0.79}Si_{0.21})_{92}$	Ho + $Au_{79}Si_{21}$	~2	~0.8	~600
HAS(CC)	$Ho_{15}(Au_{0.79}Si_{0.21})_{85}$	Ho + $Au_{79}Si_{21}$	~6	~1	~830

[a]All chemical compositions are in approximate atom %. $Au_{79}Si_{21}$ refers to a pre-arc-melted stock alloy with nominal composition $Au_{79}Si_{21}$ in atom %.

symmetry-equivalent sites (each occupied to 1/3) resulting in a 12-vertex cuboctahedron as shown in Figure 1 (far left).[6,7] The disordered tetrahedron has been the focus of numerous studies, through which it was established that under ambient conditions the disorder in the binary systems is dynamic in nature[8] and that the lowering temperature and/or increasing the pressure induces intricate transitions to ordered superstructures.[9,10]

In ternary Tsai-type 1/1 ACs, such as RE−Au−M (RE = rare-earth elements, M = p-block elements), the tetrahedron is decorated by a Au/M mixed atomic position. Hence, the tetrahedron unit is both orientationally and chemically disordered. Dynamic disorder, as observed for binary $RECd_6$ ACs, is not known for ternary systems.

There are very few reports where the disordered tetrahedron in Tsai-type phases is partially or even fully replaced by a single atom. The replacing atom is typically the largest in that specific system and is located at the cluster center: i.e., the Wyckoff position 2a. The phenomenon was first reported by Fornasini et al., who investigated the $Yb(Zn,Al)_{\sim 6}$ and $YbZn_{\sim 6}$ 1/1 ACs and showed that Yb partially, up to 70%, replaces the disordered Zn/Al tetrahedron.[11] Later, similar findings of single atoms replacing the disordered tetrahedron were reported for (Ca,Yb)−Au−Sn[12] and (Yb,Gd)−Au−Ge ACs.[13,14] Recently, we studied the Tsai-type 1/1 AC in the Tb−Au−Si system and could show that a successive replacement of the tetrahedron by a single Tb atom may be achieved by diligent control of the starting compositions and elaborate heat treatments of samples.[15] Yet, several synthesis steps were necessary for achieving a complete substitution of the tetrahedron, and although samples large enough for single-crystal X-ray diffraction could be obtained, they were not large enough or had insufficient quality to perform more elaborate physical property measurements, surface studies, or single-crystal neutron diffraction measurements. An important finding of this study, however, was that tuning the chemistry of the cluster center leads to altered magnetic properties for the Tb−Au−Si AC. It has been speculated that Tsai-type QCs containing RE elements may display unique magnetic structures on the basis of the ordering of spins in a quasiperiodic structure.[16,17] While long-range magnetic order has not yet been observed in Tsai-type QCs, several kinds of magnetic order have recently been reported for RE-containing Tsai-type ACs.[18−23] Tuning the chemistry of the Tsai cluster center may hold the key to unveiling a new family of magnetic quasicrystals and approximants and an increased understanding of magnetic order in Tsai type ACs and QCs.

This study, by taking three different 1/1 approximant systems as an example, identifies the synthesis conditions for obtaining phase-pure, single-crystalline samples of ACs where the cluster center is 100% occupied by a single RE atom. We report crystal structures and bulk magnetic properties and suggest that these compounds should be acknowledged as phases distinctly different from those of Tsai-type ACs.

II. EXPERIMENTAL SECTION

II.a. Synthesis. The starting chemicals were commercially obtained as elemental granules from Chempur (Gd, Tb, Ho, and Au, all with purity 99.99 atom %) and Highways International (Si

https://dx.doi.org/10.1021/acs.inorgchem.0c01023
Inorg. Chem. 2020, 59, 9152−9162

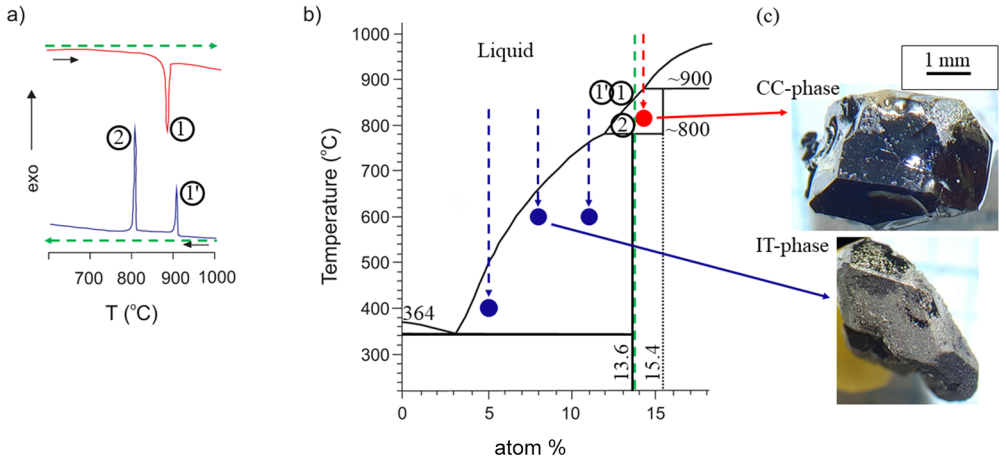

Figure 2. (a) Sketch of a DSC heating (red) and cooling (blue) trace for a conventional Tsai-type 1/1 RE−Au−Si AC (IT phase, $RE_{\sim 13.6}(Au-Si)_{\sim 86.4}$). (b) Sketch of a pseudobinary RE−($Au_{79}Si_{21}$) phase diagram containing both IT phase and pseudo-Tsai-type AC (CC phase, $RE_{\sim 15.4}(Au-Si)_{\sim 84.6}$). The green broken line and numbers 1, 1′, and 2 refer to the DSC experiment shown in Figure 2a. The arrows and circles indicate the synthesis schemes for the IT phase (blue) and CC phase (red). (c) Examples of crystal specimens separated from melts at $T > 800$ °C (CC phase, top) and $T < 600$ °C (IT phase, bottom) (cf. Figure 2b).

with purity 99.999 atom %). Alumina (Al_2O_3) crucibles, in the form of "Canfield Crucible Sets (CCS)" were obtained from LSP Industrial Ceramics.[24] The CCS consists of two 2 mL flat-bottom cylindrical crucibles and an alumina fritted disk with holes of ∼0.7−1 mm in diameter designed to separate the grains from the melt.

The binary alloy $Au_{79}Si_{21}$ was employed as the starting material. Thus, during reactions with RE the Au:Si ratio was invariant and the ternary system was considered as pseudobinary: i.e., RE−($Au_{79}Si_{21}$). The alloy was prepared by arc melting. The arc furnace was connected to high-purity Ar gas, and 5−7 g batches of the Au−Si mixture were melted on a water-cooled copper hearth. The arc furnace was flushed three times with Ar, and a titanium getter was continuously melted for ∼5 min to remove any residual oxygen before melting the samples. The samples were fully melted five times to ensure homogeneity. The total mass loss during melting was negligible (<0.4 wt %).

Six reactions, one for each sample, with the nominal compositions and weights shown in Table 1 were carried out. Samples are abbreviated as follows: Gd−Au−Si, GAS; Tb−Au−Si, TAS; Ho−Au−Si, HAS; and XXX(IT) and XXX(CC) when a Tsai phase (tetrahedron at the cluster center) and pseudo-Tsai phase (RE at the cluster center) was targeted, or represented, respectively. For each synthesis, the reactants were carefully weighed and sealed inside a glovebox (Ar atmosphere, <0.1 ppm of O_2). All reactions were carried out in CCS which were encapsulated inside stainless-steel ampules under an inert Ar atmosphere. Silica wool was inserted between the outer wall of the CCS and the inner wall of the stainless-steel tubes for thermal insulation during subsequent centrifugation after the reactions. A commercial multistep programmable muffle furnace was employed to set the temperatures for the actual reactions. Typically, ampules were first heated to 1000 °C during 10 h and kept for 10 h to ensure homogeneous melts. Then the temperature was slowly lowered (see Table 1) to allow sufficient time for crystal growth during crossing of the solidus line of the pseudobinary system. Reactions were terminated by isothermally centrifuging off excess melt.

II.b. Characterization. The samples were studied with powder X-ray diffraction (PXRD), single crystal X-ray diffraction (SCXRD), differential scanning calorimetry (DSC), scanning electron microscopy (SEM) coupled with energy dispersive X-ray spectroscopy (EDX), and magnetic property measurements. A Bruker D8 powder diffractometer with $\theta-2\theta$ diffraction geometry and a Cu Kα radiation (Kα_1 = 1.540598 Å and Kα_2 = 1.544390 Å) was used for collecting PXRD intensities at room temperature. PXRD data were analyzed with the HighScore Plus 3.0 software from PANalytical. Powdered samples were applied to a zero-diffraction plate, and diffraction patterns were measured in a 2θ range of 5−90°. In all PXRD experiments silicon powder was added as an internal standard. A Bruker D8 single-crystal X-ray diffractometer with Mo Kα radiation (Kα = 0.71073 Å) upgraded with an Incoatec Microfocus Source (IμS, beam size ∼100 μm at the sample position) and an APEX II CCD area detector (6 cm × 6 cm) was utilized to collect SCXRD intensities at room temperature. SCXRD data reduction and numerical absorption corrections were performed using the APEX III software from Bruker.[25] Both structure solution (by charge flipping) and refinements were performed using the software package JANA2006.[26] The charge-flipping algorithm incorporated in the program Superflip was used to obtain structure solutions.[27] The crystal structures were visualized using Diamond 3.2K4.[28] Electron densities were calculated from observed SCXRD intensities by Fourier methods in JANA2006 and visualized in VESTA 3.4.7.[29] DSC measurements were performed with a NETZSCH STA 449 F1 Jupiter instrument. Sample specimens (total mass 10−15 mg) were placed in a polycrystalline sapphire crucible (OD 5 mm, ID 4 mm) and a heating/cooling cycle to 1150 °C was performed at a rate of 5 °C/min under an Ar flow of ∼150 mL/min. An empty crucible served as a reference. Samples were recovered after the measurement and analyzed by PXRD. Scanning electron microscopy (SEM) investigations employed a JEOL JSM-7000F instrument equipped with a backscatter detector. Compositional analysis was performed by energy dispersive X-ray (EDX) spectroscopy, and compositional homogeneity was examined through backscatter imaging. Prior to the SEM/EDX experiments selected grains were cross section polished using an Ar^+ ion beam in a SM-09011 Cross Section Polisher instrument from JEOL. Backscattered electron images were recorded with an acceleration voltage of 20 kV and high beam current. EDX was mapped over larger areas (∼50 × ∼50 μm) for 600 s. The dc magnetization and ac susceptibility of the samples were measured as a function of temperature on an MPMS XL SQUID magnetometer from Quantum Design Inc. A magnetic field of H = 10 Oe was employed in the dc experiments, while an ac excitation with an amplitude of 4 Oe was used in the ac ones. Note that the remnant magnetic field in the magnetometer was minimized (∼−1 Oe) before collecting the magnetic data. The dc magnetization was recorded as a function of magnetic field up to ±50 kOe at T = 2 K in the same instrument.

III. RESULTS AND DISCUSSION

III.a. Synthesis of IT (Tsai) and CC (pseudo-Tsai) Phases in RE−Au−Si Systems. The composition of conventional Tsai-type 1/1 ACs in RE−Au−Si systems—possessing a $(Au/Si)_4$ tetrahedron at the center of the Tsai

https://dx.doi.org/10.1021/acs.inorgchem.0c01023
Inorg. Chem. 2020, 59, 9152−9162

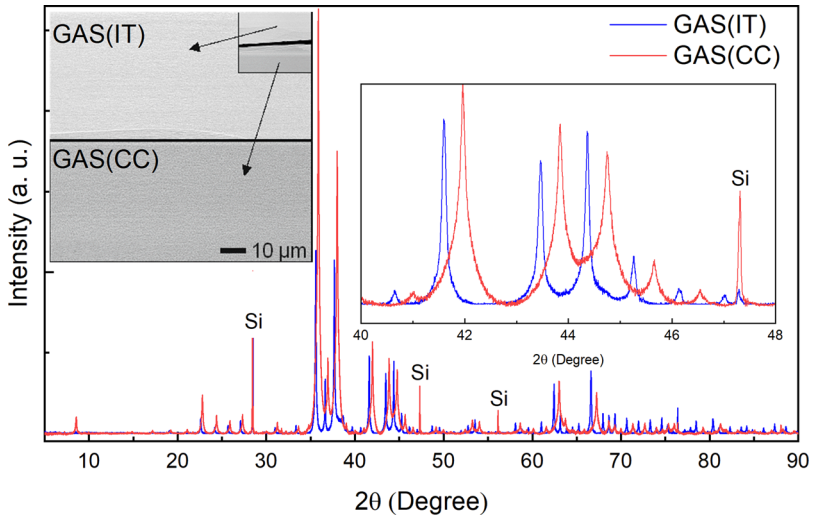

Figure 3. PXRD patterns and backscattered SEM image (upper left inset) for GAS(IT) and GAS(CC). Note that the cross section polished samples were glued together and investigated simultaneously. The lighter color indicates the lower concentration of RE for GAS(IT). The inset to the right is a close up of the PXRD patterns, emphasizing the 40−48° 2θ region. Polycrystalline silicon powder (marked as "Si") was added as an internal standard to correct for possible shifts of Bragg peaks due to experimental conditions. Diffraction background, Bragg peaks from Cu−Kα_2, and off-centering contributions have been corrected for in the plots.

cluster—is typically $RE_{\sim 13.6}(Au{-}Si)_{\sim 86.4}$;[13,30] these ACs are herein referred to as IT phases (inner tetrahedron). The proportion of Au:Si in the IT phases is close to 4:1, and coincidentally, this ratio corresponds closely to the eutectic composition in the binary Au−Si system ($Au_{79}Si_{21}$).[31] The melting point of the eutectic is extraordinarily low, ∼364 °C, and thus—considering the systems as pseudobinary, i.e. RE-($Au_{79}Si_{21}$)—ideal conditions are provided for the flux growth of IT phase crystals from $Au_{79}Si_{21}$-rich melts. In this work pure samples of millimeter-sized IT phase crystals were synthesized from melts containing between 5 and 11% RE.

The common existence of AC phases with altered Tsai clusters in RE−Au−Si systems, i.e. with the central tetrahedron replaced by a single RE atom (herein denoted CC or pseudo-Tsai phases), was first suspected from DSC investigations of IT phases. Experiments would show one pronounced thermal event upon heating but two distinct events upon cooling. The DSC traces of these heating−cooling cycles are sketched in Figure 2a. The behavior was interpreted as such that, upon heating, the melting of the IT phase is observed. Upon cooling, melts with composition $RE_{\sim 13.6}(Au{-}Si)_{\sim 86.4}$ form a CC phase (with composition $RE_{\sim 15.4}(Au{-}Si)_{\sim 84.6}$, see discussion below) and a Au−Si-richer melt when the solidus line was crossed. The second thermal event corresponds to the peritectic formation of the IT phase from the melt and CC phase. PXRD patterns of samples after a DSC heating−cooling cycle showed significantly broadened and/or split peaks, indicating the presence of two AC phases with different cell parameters (such PXRD patterns are shown in Figure S1 in the the Supporting Information). This interpretation implies that the peritectic decomposition of the IT phase into melt and CC phase is comparatively slow, or even kinetically hindered, in comparison to its peritectic formation upon cooling. A sketch of a pseudobinary phase diagram containing both IT phase and CC phase and indicating the thermal events of the DSC experiment is shown in Figure 2b.

The phase diagram sketch has been subsequently used as a guide for synthesis. Pure samples of millimeter-sized CC phase crystals were synthesized from melts containing ∼14% RE which were slowly cooled to T > 800 °C and subsequently centrifuged (red arrow in Figure 2b). The corresponding synthesis procedure for the IT phases is indicated as blue arrows in Figure 2b. Figure 2c depicts examples of crystals obtained after melt centrifugation.

The compositional difference between the IT and CC phases is clearly revealed in EDX analysis on a cross section polished crystal specimen. Further, CC phases have a smaller cubic lattice parameter (by 0.6−0.8%) in comparison to their corresponding IT phases. Figure 3 shows examples of the PXRD patterns and backscattered SEM images of the IT and CC phases in the GAS system. Similar plots for the TAS and HAS systems are given in Figure S2 in the Supporting Information. EDX gives the compositions $Gd_{15.4(4)}Au_{68.6(3)}Si_{16.0(3)}$ and $Gd_{13.7(3)}Au_{72.7(3)}Si_{13.6(3)}$ for GAS(CC) and GAS(IT), respectively, which are very close to the expected values from the structure refinement (see section III.b). The compositional difference of GAS(CC) and GAS(IT) is manifested as a contrast difference in the backscattered electron image. The lattice parameters for GAS(CC) and GAS(IT) are 14.5781(18) and 14.7014(13) Å, respectively. EDX compositions and lattice parameters for all compounds are given in Table 1. Although we explicitly show the existence of a CC phase only for RE−Au−Si (RE = Gd, Tb, Ho), it is inferred that this phase is generally present in RE−Au−M (M = p element) systems.

III.b. Atomic Structures of the IT and CC Phases. Both IT and CC phases crystallize in the space group $Im\bar{3}$ and contain two clusters in the unit cell. Figure 1 shows the Tsai cluster of the conventional Tsai-type 1/1 AC GAS(IT). The cluster midpoints coincide with the corners and the body center of the cubic unit cell (Wyckoff position 2a), and clusters interpenetrate through their fourth (rhombic-triacontahedron) shell. The structures of TAS(IT) and HAS(IT) are virtually identical with that of GAS(IT). All have orientationally disordered $(Au/Si)_4$ tetrahedral units at the cluster center defined by a 12-vertex cuboctahedron through a position 24g that has a total occupancy of 1/3, which is constrained as such during refinement. The Au:Si ratio for this position (Au7/Si7)

https://dx.doi.org/10.1021/acs.inorgchem.0c01023
Inorg. Chem. 2020, 59, 9152−9162

Table 2. Crystallographic Data Obtained from SCXRD Refinements and EDX Results

param	compd					
	GAS(CC)	TAS(CC)	HAS(CC)	GAS(IT)	TAS(IT)	HAS(IT)
ref comp	$Gd_{1.08}Au_{4.73(1)}Si_{1.25(2)}$	$Tb_{1.08}Au_{4.76(2)}Si_{1.20(2)}$	$Ho_{1.08}Au_{4.75(2)}Si_{1.25(2)}$	$Gd_{1.00}Au_{5.02(2)}Si_{1.32(2)}$	$Tb_{1.00}Au_{4.91(2)}Si_{1.42(2)}$	$Ho_{1.00}Au_{4.93(1)}Si_{1.40(1)}$
norm comp (%)	$Gd_{15.3}Au_{67.0(2)}Si_{17.7(3)}$	$Tb_{15.3}Au_{67.6(3)}Si_{17.1(3)}$	$Ho_{15.3}Au_{67.1(3)}Si_{17.6(3)}$	$Gd_{13.6}Au_{68.4(2)}Si_{18.0(2)}$	$Tb_{13.6}Au_{67.0(3)}Si_{19.4(3)}$	$Ho_{13.6}Au_{67.2(2)}Si_{19.2(2)}$
EDX comp (%)	$Gd_{15.4(4)}Au_{68.6(3)}Si_{16.0(3)}$	$Tb_{15.0(4)}Au_{70.4(7)}Si_{14.6(4)}$	$Ho_{15.7(9)}Au_{68.3(7)}Si_{16.0(4)}$	$Gd_{13.7(3)}Au_{72.7(3)}Si_{13.6(3)}$	$Tb_{14.0(5)}Au_{69.0(4)}Si_{17.0(2)}$	$Ho_{13.8(4)}Au_{69.4(4)}Si_{16.9(4)}$
molar mass (g/mol)	1137.4	1143.8	1148.4	1182.4	1165.8	1175.4
temp of measmt (K)	293	293	293	293	293	293
space group	$Im\bar{3}$	$Im\bar{3}$	$Im\bar{3}$	$Im\bar{3}$	$Im\bar{3}$	$Im\bar{3}$
a axis (Å)	14.5781(18)	14.549(3)	14.4599(12)	14.7014(13)	14.6525(17)	14.6525(17)
cell vol (Å^3)	3098.2	3079.8	3023.4	3177.4	3145.8	3145.8
Z	24	24	24	24	24	24
calcd density (g/cm^3)	14.6309	14.8011	15.1375	14.8302	14.7693	14.8907
cryst color	metallic gray	metallic gray	metallic gray	metallic gray	metallic gray	metallic gray
abs coeff (mm^{-1})	147.771	150.424	154.581	150.936	150.309	152.492
no. of indep rflns	941	946	915	972	944	945
no. of obsd rflns ($I > 3\sigma(I)$)	881	838	866	908	691	887
R_{int} (obsd/all)	5.19/5.20	4.37/4.42	4.87/4.88	5.46/5.47	7.53/8.07	3.51/3.53
no. of ref params	93	93	93	92	92	92
redundancy	14.91	14.62	18.793	19.094	14.62	18.458
R1 (obsd/all)	0.0336/0.0357	0.0369/0.0423	0.0278/0.0299	0.0328/0.0352	0.0299/0.0458	0.0221/0.0241
wR2 (obsd/all)	0.0927/0.0930	0.0922/0.0935	0.0772/0.0780	0.0764/0.0769	0.0592/0.0620	0.0544/0.0548
GOF on F^2 (obsd/all)	3.41/3.29	3.54/3.35	2.59/2.54	2.91/2.82	1.46/1.29	2.43/2.37
$\Delta\rho_{max}$, $\Delta\rho_{min}$ (e/A^3)	7.34, −4.00	4.61, −6.49	2.67, −7.34	4.81, −3.27	4.15, −2.92	2.90, −1.73

https://dx.doi.org/10.1021/acs.inorgchem.0c01023
Inorg. Chem. 2020, 59, 9152−9162

is ~3:2. In GAS(CC), TAS(CC), and HAS(CC) the central tetrahedron is fully replaced by a single fully occupied RE atom. This is clearly revealed in the SCXRD data, where the electron density maps at low isolevels (13 e/Å^3) show no trace of tetrahedral residues while the central RE density is clearly visible. The residual electron densities around the cluster center are comparably low for such a complex structure with heavy elements, which indicates that the CC phases are well and fully described by the presence of a single RE atom inside the dodecahedral cavity. The structure refinement results for the investigated IT and CC phases are compiled in Table 2 and Table S1 in the Supporting Information. Moreover, all structures have been deposited in the ICSD crystallographic database. Refined total atomic compositions are in good agreement with EDX results for all refinements. The differences are in the ranges 0.1−0.4 atom % for RE, 1.2−4.4 atom % for Au and 1.6−4.3 atom % for Si.

Figure 4 shows electron density isosurface plots around the cluster centers and the dodecahedron shell for GAS(IT) and GAS(CC). Similar plots for TAS and HAS systems are shown in Figure S3 in the Supporting Information, . The electron densities were obtained from observed SCXRD intensities and calculated from standard Fourier synthesis after the final structure refinement. The generated ".PGRID" file for each structure is provided as Supporting Information. For GAS(IT) the observed electron density around the cluster center corresponds to the disordered $(Au/Si)_4$ tetrahedron and there is no electron density at the exact cluster center 2a position. Vice versa, for GAS(CC) the electron density is concentrated at the exact cluster center (position corresponding to Gd2), whereas the area where the $(Au/Si)_4$ tetrahedron located in GAS(IT) is void of electron density.

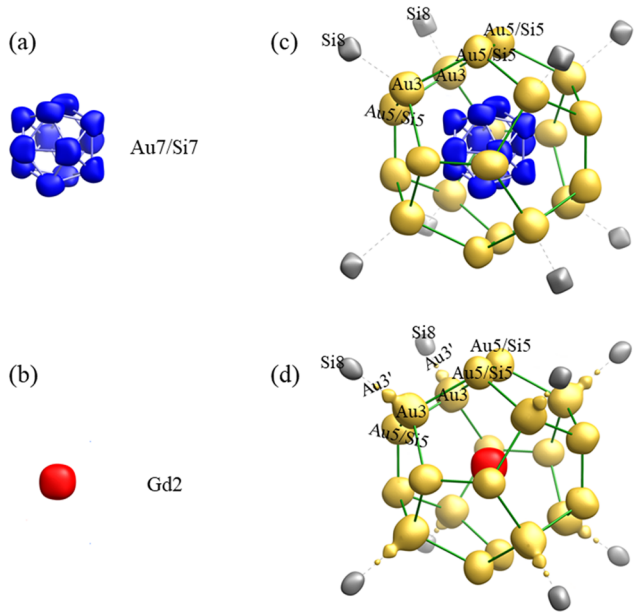

Figure 4. Electron density isosurfaces near the cluster center for (a) GAS(IT) and (b) GAS(CC) and an expanded region including the dodecahedron shell for (c) GAS(IT) and (d) GAS(CC). Isosurfaces in blue, red, gray, and gold are from Au7/Si7 mixed sites of the disordered tetrahedron, Gd2 sites, Si8 sites and dodecahedral shell atoms, respectively. (d) Elongated electron density from the Au3/Au3′ split site of GAS(CC). The equivalent Au3 site in GAS(IT) is spherical. Isosurfaces were obtained by standard Fourier maps using the observed SCXRD intensities. The isosurface level was set at 13 e/Å^{-3}.

Replacing the relatively larger $(Au/Si)_4$ tetrahedron with a single RE atom introduces positional disorder on other atomic sites in the CC phase. Interatomic distances on the dodecahedral shell appear reduced from ~2.74 Å (Au3−Au5/Si5) and ~2.34 Å (Au5/Si5−Au5/Si5) to ~2.62 Å and ~2.23 Å, respectively, when GAS(IT) is compared with GAS(CC). A significant atomic displacement is particularly observed on a Au atom (Au3 in Table S1 in the Supporting Information) at the dodecahedral shell (first shell in Figure 1). Large atomic displacement parameters and elongated electron densities in the ⟨111⟩ crystallographic directions were observed. Figure 4 shows the observed electron density isosurface near the dodecahedron shell for the GAS phases. A better structure refinement (lower R1, wR2 and GOF values in Table 2) was obtained when the Au3 atom was modeled as the two split positions Au3 and Au3′, with the sum of occupancies for these two positions restricted to unity in the CC phase. The new Au3′ position is very close to the Si8 site located at 1/4,1/4,1/4, resulting in unphysically short interatomic distances between Au3′ and Si8 sites (~1.42 Å for GAS(CC)). We therefore conclude that these two sites are mutually exclusive, meaning that one cannot exist in the presence of the other. Therefore, the occupancy of the position Si8 in the CC phase was refined with the condition that the site must be vacant when the Au3′ site is occupied. For the IT phase compounds the Si8 site is fully occupied and there is no Au3′ site (only a fully occupied Au3 position). Our physical interpretation of the Au3−Au3′ splitting is based on the fact that we can only directly observe an electron density distribution which is a weighted average of two distinctly different local environments in the crystal: occupied and vacant sites of the Si8 atom. Whenever the Si8 atom is present, the adjacent Au atoms move to the more distant Au3 positions to achieve physically sound Au−Si distances (~2.714, ~2.792, and ~2.709 Å for the Au3−Si8 pairs in the GAS(CC), TAS(CC), and HAS(CC) structures, respectively), while the same Au atoms relax to the Au3′ positions only around vacant Si8 sites. Another question is why vacant Si8 sites are only encountered in the CC phases and not in the IT phases. We can at present only speculate about the driving force behind the Si8 vacancy formation at the 1/4,1/4,1/4 position. However, it is known from the prototypic binary RE−Cd approximants that this position (also known as a Cd_8 cube interstitial site) can host additional atoms only in ACs with RE atoms equal in size or larger than Pr,[32] while these positions are vacant for the ACs with smaller RE atoms. This indicates that the relative atomic size of the RE which affects the size of the unit cell (and therefore interatomic distances) will have an effect on this occupancy. The unit cell of the CC phases is consistently smaller than that of the IT phases, and a similar shrinkage of the unit cell is also observed for RE−Cd approximants as the radius of the RE atom diminishes. We therefore believe that the replacement of tetrahedral moieties by single RE atoms at the cluster centers causes a shrinkage of the structure that favors vacancy formation.

The disordered-tetrahedral unit is the only icosahedral symmetry breaking unit among the atomic shells of the Tsai cluster. It has internally restricted Tsai-type QCs and ACs from possessing full local icosahedral symmetry. Replacing the tetrahedral unit with a single atom lifts this restriction, which in

https://dx.doi.org/10.1021/acs.inorgchem.0c01023
Inorg. Chem. 2020, 59, 9152−9162

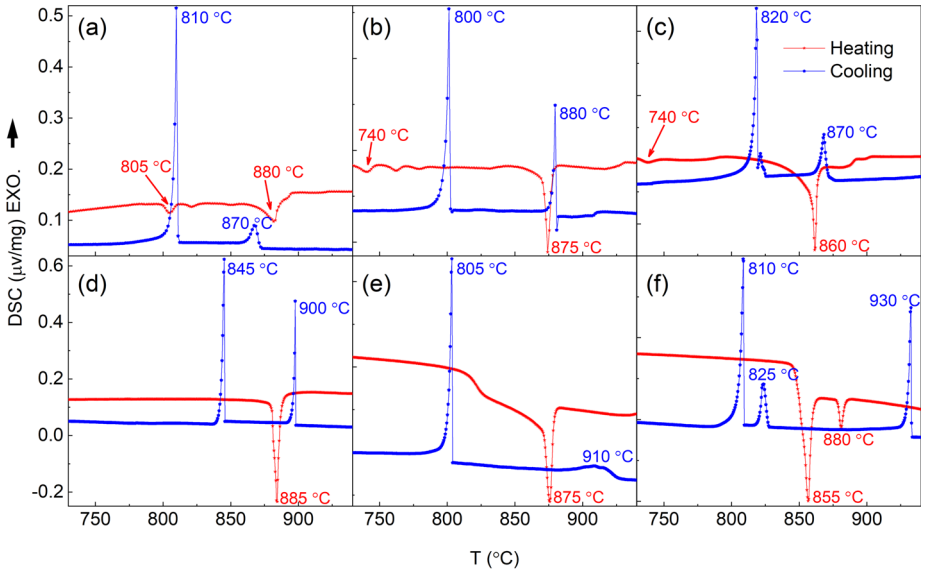

Figure 5. Plots for DSC results of the IT compounds (a) GAS(IT), (b) TAS(IT), (c) HAS(IT) and the CC compounds (d) GAS(CC), (e) TAS(CC), and (f) HAS(CC). Temperatures of endothermic (downward ↓) and exothermic (upward ↑) events are indicated.

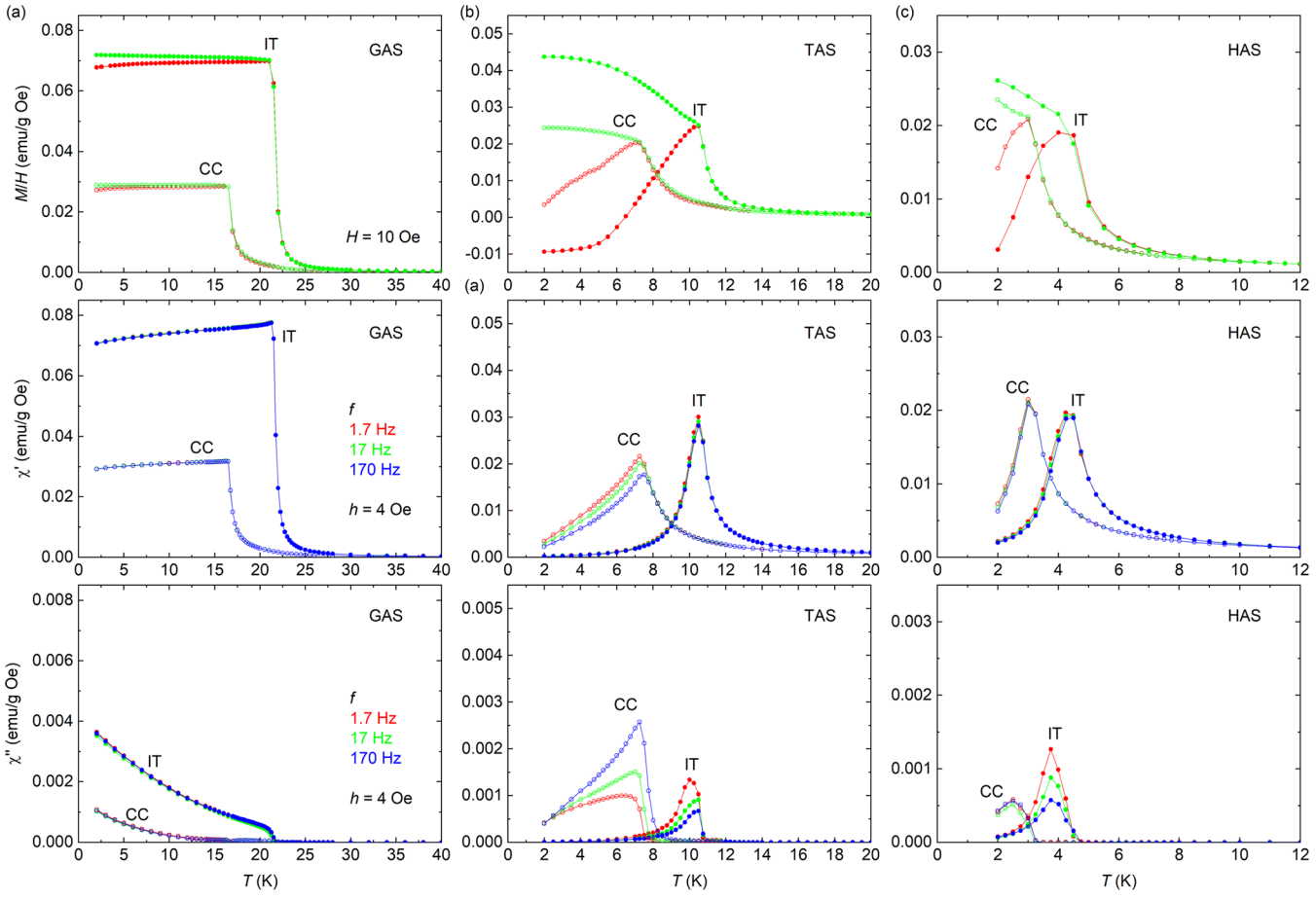

Figure 6. Magnetic properties of IT (filled circles) and CC phases (open circles) at low temperatures: (a) GAS; (b) TAS; (c) HAS. Upper panels: temperature dependence of the ZFC (red) and FC (green) magnetization M (plotted as M/H) recorded in the applied magnetic field H = 10 Oe. Middle and bottom panels: temperature dependence of the in-phase (middle panels) and out-of-phase (bottom panels) components of the ac magnetic susceptibility recorded using the ac excitation H = 4 Oe at frequencies f = 1.7 (red), 17 (green), 170 Hz (blue). Note that some of the curves were phase-compensated.

principle could lead to the formation of quasicrystals with full icosahedral symmetry both locally and overall.

III.c. Thermal Analysis of IT and CC Phases. As initially mentioned, the existence of the CC phase in ternary RE−Au−

https://dx.doi.org/10.1021/acs.inorgchem.0c01023
Inorg. Chem. 2020, 59, 9152−9162

Si phase systems was first recognized from DSC measurements. Figure 5 compiles DSC thermograms for the IT and CC phases of the investigated RE−Au−Si systems (GAS(IT), GAS(CC), TAS(IT), TAS(CC), HAS(IT), HAS(CC)) during a heating−cooling cycle. In all cases a complete melt was achieved at the highest temperature, 1150 °C. Generally, heating traces of the IT phases show one prominent endothermic event between 860 and 880 °C, which is assigned to melting (cf. the phase diagram sketch, Figure 2b). Smaller endothermic peaks prior may be related to peritectic decomposition into CC phase and melt and/or order−disorder transitions arising from the central tetrahedron unit. Notably, such smaller peaks prior to the prominent endothermic event are absent in the heating traces of the CC phases.

The thermal behavior of GAS and TAS is in qualitative agreement with the phase diagram sketch shown in Figure 2b, when it is assumed that peritectic decompositions upon heating generally are too slow to be resolved in DSC experiments: GAS(IT) melts at 870−880 °C and forms peritectically at 810 °C. GAS(CC) melts at ∼890−900 °C and forms peritectically at 845 °C. TAS(IT) melts at 875−880 °C and forms peritectically at 800 °C. TAS(CC) melts at 875−910 °C and forms peritectically at 805 °C. Also, HAS(IT) follows this simplified picture, with melting at 860−865 °C and peritectic formation at 820 °C. The thermal behavior of HAS(CC), however, is clearly more complicated, showing two events upon heating and three upon cooling. The temperature difference between the melting point (solids) of the IT phase composition and the peritectic formation of the IT phase has been exploited for the synthesis of the CC phase. It is not yet clear whether the CC phases are thermodynamically stable at low temperatures or represent high-temperature phases. Annealing experiments at 600 °C for 1 month did not indicate decomposition for GAS(CC) and TAS(CC), whereas slight changes in the PXRD pattern of HAS(CC) could be observed, as shown in Figure S4 in the Supporting Information.

It is important to point out that our strategy does not provide any information whether the region 13.6 < atom % RE < 15.4 in the RE−Au−Si phase diagram is a two-phase region or rather represents a solid solution. Our previous study of the Tb−Au−Si system indicates a solid solution behavior, at least for RE = Tb.[15]

III.d. Magnetic Property Measurements. ACs play an important role in elucidating the atomic structures of QCs. Similarly, the study of their magnetic properties is expected to help in understanding the magnetic order in aperiodic QCs.[23,33] In this respect, the study of TAS has been especially fruitful. Recently, Hiroto et al. presented a complete magnetic structure solution from single-crystal neutron diffraction data for TAS(IT) showing intricate noncollinear and noncoplanar ferrimagnetic-like ordering on the icosahedral Tb shell of the Tsai cluster.[21] Further, Gebresenbut et al. showed that a successive replacement of the central tetrahedron unit in the Tsai cluster by a single Tb atom leads to a lowering of the magnetic ordering temperature.[15] However, millimeter-sized single crystals of TAS(CC) synthesized from excess flux as in the present case were not available at the time.

The dc magnetic properties of IT and CC phases are compared in Figure 6 (top row). In all three systems studied here, the magnetization is found to rise sharply as the temperature decreases. For TAS and HAS, the shape of the magnetization curves is reminiscent of those of ferrimagnets.[34,35] The onset of magnetic ordering is somehow less sharp for TAS(CC) than for TAS(IT). On the other hand, the ZFC-FC curves of GAS seem to be significantly different from those of TAS and HAS; the GAS systems exhibit sharper, ferromagnetic-like onsets of magnetic ordering, and the difference between ZFC and FC curves is not as significant as that between TAS and HAS. The flat susceptibility curves of the GAS systems at low temperatures suggest that the measured susceptibility is limited by demagnetizing effects (e.g., for GAS(CC), the susceptibility is about 0.03 emu/g Oe, which corresponds to the SI value of 5.65 or $1/N$ with $N \approx 0.18$). We define T_{mag} as the temperature for the maximum slope of the susceptibility for all samples except for TAS(CC), for which we define T_{mag} as the temperature of the maximum in the ZFC magnetization. The experimental values of T_{mag} are given in Table 3. The magnetic-ordering temperatures T_{mag} of

Table 3. Compilation of Magnetic Property Data

sample	T_{mag} (K)	Θ_P (K)	p_{eff} (μ_B/RE)/$g_J\sqrt{J(J+1)}$ (estimated in 50 $\lesssim T \lesssim$ 300 K)	M(50 kOe, 2 K) (μ_B/RE)/$g_J J$
GAS(IT)	21.8	24.4	8.01/7.94	6.99/7
GAS(CC)	16.8	15.7	8.04/7.94	6.33/7
TAS(IT)	10.9	10.2	9.86/9.72	5.24/9
TAS(CC)	7.3	5.9	9.84/9.72	5.26/9
HAS(IT)	4.8	2.3	10.85/10.58	6.30/10
HAS(CC)	3.4	1.5	11.02/10.58	7.04/10

the IT phases are systematically higher than those of the corresponding CC phases. The IT phases have been investigated previously, and our results are in good agreement with the previous studies.[13,23,33] In particular, GAS(IT) was compared with Gd−Au−Ge 1/1 AC, and the latter exhibits a frequency-dependent ac susceptibility.[33] As revealed in this study, GAS(IT) and GAS(CC) do not exhibit clear frequency dependence in the ac magnetic susceptibility, suggesting that the type of magnetic transition of GAS may be different from that of the Gd−Au−Ge 1/1 AC.

The in- and out-of-phase components of the ac susceptibility data for TAS(IT), HAS(IT), and HAS(CC) are compatible with that of ferro-/ferrimagnets, with a sharp peak around T_{mag} in both components. However, it can be seen in Figure 6, e.g. in the out-of-phase component data, that the sharp peak is accompanied by some frequency dependence below T_{mag}, which may reflect slow relaxation inherent to the complex magnetic order determined by recent neutron-scattering experiments for such systems.[21] TAS(CC) exhibits, however, a strikingly different behavior, as the temperature onset of magnetic ordering is found to significantly depend on the frequency, in a spin-glass-like way,[36] suggesting a short-range and glassy magnetic order for this system. The temperature onset of ordering seems sharper (long-range) in an earlier crystal of TAS(CC),[15] however. We have checked that the ac susceptibility of that crystal is qualitatively similar to that of our present TAS(CC): i.e., it reflects a glassy behavior.

In spite of ferrimagnetic-like ordering, we observe a linear Curie−Weiss law temperature dependence of the inverse susceptibility surprisingly down to low temperature, as low as just above T_{mag} for both systems (see Figure S5 in the Supporting Information); this feature indicates that the present magnetic systems are distinguished from the ordinary ferrimagnets.[34] That feature indicates that the 4f electrons are well localized in a wide temperature range and the present

https://dx.doi.org/10.1021/acs.inorgchem.0c01023
Inorg. Chem. 2020, 59, 9152−9162

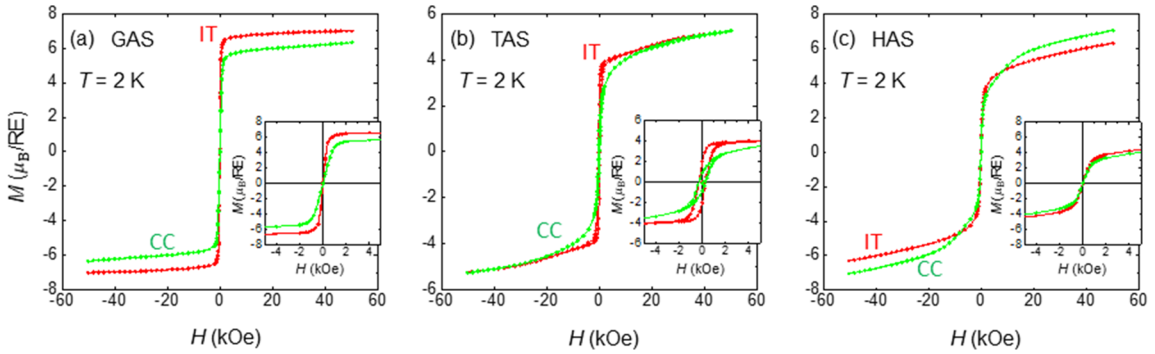

Figure 7. Magnetic-field dependence of the magnetization of IT (red) and CC (green) systems recorded at T = 2 K (M plotted in μ_B/RE, RE = Gd, Tb or Ho): (a) GAS; (b) TAS; (c) HAS. The insets show close-up views of the low-field region. RE denotes the rare-earth elements (RE = Gd, Tb, Ho).

systems would be classified into the group of localized-electron magnetic systems. For information, the extracted Curie–Weiss temperatures Θ_P (estimated in the temperature interval of 50 $\lesssim T \lesssim$ 300 K) are given in Table 3. The values of effective magnetic moments (p_{eff}) extracted from the experimental data are given in Table 3, and the values are in good agreement with the theoretical $g_J\sqrt{J(J+1)}$ values, where g_J is the Lande g factor.

TAS and HAS show similar magnetic behavior in their IT phases. In both cases, the temperature onset of magnetic ordering and Θ_P were found to decrease in the CC phases. However, TAS(CC) and HAS(CC) exhibit significant differences in their ac magnetic response. This suggests that the rare-earth magnetic state/order on icosahedral sites is more or less similar but the cluster-center rare-earth contributions to the magnetic states are significantly different between TAS and HAS; the cluster-center Tb^{3+} moments yield magnetic frustration/disorder and glassiness in the TAS(CC) system.

Figure 7 shows the magnetic-field dependence of magnetization M measured at T = 2 K. The M–H curves of GAS systems are soft-ferromagnetic-like. Note that the magnetization values at H = 50 kOe are given in Table 3. The difference in the slope of M–H curves at the low-field region for the IT and CC systems should be ascribed to the demagnetization effect. In GAS(IT), we observe an almost complete saturation of M with a value close to the theoretical value of g_JJ = 7 μ_B/Gd^{3+} at H = 50 kOe, where μ_B is the Bohr magneton. In the case of TAS and HAS, the M–H curves of both materials are ferrimagnetic-like for the IT and CC phases, with no saturation up to 50 kOe. The magnetization M (H = 50 kOe) amounts to ~5.2–5.3 μ_B/Tb for TAS and 6.3–7.0 μ_B/Ho for HAS, respectively. These high-field magnetization values are smaller than the theoretical values of g_JJ = 9 μ_B/Tb^{3+} and g_JJ = 10 μ_B/Ho^{3+}; this can be ascribed to the crystal-electric-field effect. Also, the M–H curves may reflect the complex magnetic structure of the material, with a resulting moment of about ~4 μ_B/RE (estimated near H = 0). As mentioned above, the coercivity of the TAS(IT) at low temperatures is relatively large (~250 Oe at 2 K), as observed earlier[15] and as suggested by the negative ZFC magnetization observed at low temperatures for this sample (see Figure 6b). The coercivity at the same temperature is much lower for HAS systems; however, the measurement temperature is closer to T_{mag} in that case.

IV. CONCLUSIONS

The atomic structures, formation conditions, compositions, and temperatures for Tsai and pseudo-Tsai type 1/1 ACs in the RE–Au–Si (RE = Gd, Tb, Ho) systems have been determined. Tsai (IT phase) refers to the more prevalent compounds where a tetrahedral moiety is at the center of the atomic cluster, whereas pseudo-Tsai (CC phase) refers to the case where a RE atom fully replaces the tetrahedron. In both cluster types concentric atomic shells of a dodecahedron, an icosahedron, an icosi-dodecahedron, and a triacontahedron surround the central units. A schematic partial pseudobinary phase diagram between RE and $Au_{79}Si_{21}$ was proposed and used as a guide to prepare large (several millimeters) single crystals of both Tsai and pseudo-Tsai phases. We speculate that the existence of pseudo-Tsai phases is a more general phenomenon that occurs in more systems than those presented here, and hence they should be acknowledged as an independent group of compounds that is structurally similar yet physically different from Tsai phases.

All the compounds investigated herein have shown ferro- or ferrimagnetic-like ordering at low temperatures, except TAS-(CC), which exhibits a spin-glass-like behavior. However, the temperature onsets of ordering were found to shift to lower temperatures for the CC phases in comparison to their IT-counterparts; for GAS, TAS, and HAS systems T_{mag} shifts from ~22 to 17 K, ~11 to 7 K, and ~5 to 3.5 K, respectively. Now that firm procedures for the upscaled synthesis of phase-pure pseudo-Tsai phases have been established, the door stands open for the exploration of physical properties, atomic surfaces, magnetic structures, and non-Fermi liquid properties of these compounds that exist alongside their Tsai counterparts with crucially different physical properties. Furthermore, the possibility emerges of the parallel existence of pseudo-Tsai type quasicrystals with properties yet unknown.

■ ASSOCIATED CONTENT

Supporting Information

The Supporting Information is available free of charge at https://pubs.acs.org/doi/10.1021/acs.inorgchem.0c01023.

Atomic coordinates and temperature parameters, PXRD results of DCS run specimen for each sample, PXRD and SEM results for TAS and HAS systems, electron density isosurface plots for TAS and HAS systems, PXRD patterns of samples before and after annealing, and temperature dependence of the inverse magnetic susceptibility for all compounds (PDF)

https://dx.doi.org/10.1021/acs.inorgchem.0c01023
Inorg. Chem. 2020, 59, 9152–9162

Accession Codes

CCDC 1995334−1995339 contain the supplementary crystallographic data for this paper. These data can be obtained free of charge via www.ccdc.cam.ac.uk/data_request/cif, or by emailing data_request@ccdc.cam.ac.uk, or by contacting The Cambridge Crystallographic Data Centre, 12 Union Road, Cambridge CB2 1EZ, UK; fax: +44 1223 336033.

AUTHOR INFORMATION

Corresponding Authors

Girma Gebresenbut − *Department of chemistry, Ångström laboratory, Uppsala University, 751 21 Uppsala, Sweden;* orcid.org/0000-0003-1804-8259; Email: girma.gebresenbut@kemi.uu.se

Cesar Pay Gómez − *Department of chemistry, Ångström laboratory, Uppsala University, 751 21 Uppsala, Sweden;* Email: cesar.paygomez@kemi.uu.se

Authors

Takayuki Shiino − *Department of materials science and engineering, Uppsala University, 751 21 Uppsala, Sweden*

Daniel Eklöf − *Department of materials and environmental chemistry, Stockholm University, 106 91 Stockholm, Sweden*

Deep Chandra Joshi − *Department of materials science and engineering, Uppsala University, 751 21 Uppsala, Sweden*

Fernand Denoel − *Department of materials science and engineering, Uppsala University, 751 21 Uppsala, Sweden*

Roland Mathieu − *Department of materials science and engineering, Uppsala University, 751 21 Uppsala, Sweden;* orcid.org/0000-0002-5261-2047

Ulrich Häussermann − *Department of materials and environmental chemistry, Stockholm University, 106 91 Stockholm, Sweden;* orcid.org/0000-0003-2001-4410

Complete contact information is available at: https://pubs.acs.org/10.1021/acs.inorgchem.0c01023

Author Contributions

The manuscript was written through contributions of all authors. All authors have given approval to the final version of the manuscript.

Funding

We thank the Knut and Alice Wallenberg Foundation (grant number KAW 2018.0019), the Carl Tryggers Stiftelse för Vetenskaplig Forskning (grant number CTS 19:235), Stiftelsen Olle Engkvist Byggmästare and the Swedish Research Council (VR) Dnr: 349-2014-3946.

Notes

The authors declare no competing financial interest.

ABBREVIATIONS

QCs, quasicrystals; ACs, approximants of quasicrystals; RE, rare-earth elements; PXRD, powder X-ray diffraction; SCXRD, single-crystal X-ray diffraction; DSC, differential scanning calorimetry; SEM, scanning electron microscopy; EDX, energy dispersive X-ray; GAS, Gd−Au−Si, TAS, Tb−Au−Si; HAS, Ho−Au−Si; T_{mag}, magnetic ordering temperature

REFERENCES

(1) Shechtman, D.; Blech, I.; Gratias, D.; Cahn, J. Metallic phase with long-range orientational order and no translational symmetry. *Phys. Rev. Lett.* **1984**, *53* (20), 1951−1953.

(2) Yamamoto, A. Crystallography of quasiperiodic crystals. *Acta Crystallogr., Sect. A: Found. Crystallogr.* **1996**, *52* (4), 509−560.

(3) Takakura, H.; Pay Gómez, C.; Yamamoto, A.; De Boissieu, M.; Tsai, A. p. Atomic structure of the binary icosahedral Yb-Cd quasicrystal. *Nat. Mater.* **2007**, *6* (1), 58−63.

(4) Goldman, A.; Kelton, R. Quasicrystals and crystalline approximants. *Rev. Mod. Phys.* **1993**, *65* (1), 213−230.

(5) Tsai, A.; Guo, J.; Abe, E.; Takakura, H.; Sato, T. A stable binary quasicrystal. *Nature* **2000**, *408* (6812), 537−538.

(6) Larson, A.; Cromer, D. The Crystal Structure of YCd_6. *Acta Crystallogr., Sect. B: Struct. Crystallogr. Cryst. Chem.* **1971**, *27* (10), 1875−1879.

(7) Pay Gómez, C.; Lidin, S. Comparative structural study of the disordered MCd_6 quasicrystal approximants. *Phys. Rev. B: Condens. Matter Mater. Phys.* **2003**, *68* (2), 024203.

(8) Euchner, H.; Yamada, T.; Rols, S.; Ishimasa, T.; Kaneko, Y.; Ollivier, J.; Schober, H.; Mihalkovic, M.; de Boissieu, M. Tetrahedron dynamics in the icosahedral quasicrystals i-ZnMgSc and i-ZnAgSc and the cubic 1/1-approximant Zn_6Sc. *J. Phys.: Condens. Matter* **2013**, *25* (11), 115405.

(9) Tamura, R.; Nishimoto, K.; Takeuchi, S.; Edagawa, K.; Isobe, M.; Ueda, Y. Universal low-temperature phase transition in Zn- and Cd-based crystalline approximants. *Phys. Rev. B: Condens. Matter Mater. Phys.* **2005**, *71* (9), 092203.

(10) Watanuki, T.; Machida, A.; Ikeda, T.; Aoki, K.; Kaneko, H.; Shobu, T.; Sato, T.; Tsai, A. p. Pressure-induced phase transitions in the Cd-Yb periodic approximant to a quasicrystal. *Phys. Rev. Lett.* **2006**, *96* (10), 105702.

(11) Fornasini, M.; Manfrinetti, P.; Mazzone, D.; Dhar, S. Crystal structure and magnetic properties of the compounds $Yb(Zn, Al)_{\sim 6}$ and $YbZn_{\sim 6}$. *Z. Naturforsch., B: J. Chem. Sci.* **2008**, *63b*, 237−243.

(12) Lin, Q.; Corbett, J. $M_3(Au, Ge)_{19}$ and $M_{3.25}(Au, Ge)_{18}$ (M = Ca, Yb): Distinctive phase separations driven by configurational disorder in cubic YCd_6-type derivatives. *Inorg. Chem.* **2010**, *49* (10), 4570−4577.

(13) Gebresenbut, G.; Tamura, R.; Eklöf, D.; Pay Gómez, C. Syntheses optimization, structural and thermoelectric properties of 1/1 Tsai-type quasicrystal approximants in RE−Au−SM systems (RE = Yb, Gd and SM = Si, Ge). *J. Phys.: Condens. Matter* **2013**, *25* (13), 135402.

(14) Taguchi, T.; So, Y. Direct observation of the local atomic structure in two types of Au-Ge-Yb 1/1 approximants. *J. Phys.: Conf. Ser.* **2020**, *1458*, 012005.

(15) Gebresenbut, G.; Andersson, M.; Nordblad, P.; Sahlberg, M.; Pay Gómez, C. Tailoring magnetic behavior in the Tb-Au-Si quasicrystal approximant system. *Inorg. Chem.* **2016**, *55* (5), 2001−2008.

(16) Goldman, A. Magnetism in icosahedral quasicrystals: current status and open questions. *Sci. Technol. Adv. Mater.* **2014**, *15* (4), 044801.

(17) Goldman, A.; Kong, T.; Kreyssig, A.; Jesche, A.; Ramazanoglu, M.; Dennis, K.; Bud'ko, S.; Canfield, P. A family of binary magnetic icosahedral quasicrystals based on rare earths and cadmium. *Nat. Mater.* **2013**, *12* (8), 714−8.

(18) Sato, T.; Ishikawa, A.; Sakurai, A.; Hattori, M.; Avdeev, M.; Tamura, R. Whirling spin order in the quasicrystal approximant $Au_{72}Al_{14}Tb_{14}$. *Phys. Rev. B: Condens. Matter Mater. Phys.* **2019**, *100* (5), 054417.

(19) Miyazaki, H.; Sugimoto, T.; Morita, K.; Tohyama, T. Magnetic orders induced by RKKY interaction in Tsai-type quasicrystalline approximant Au-Al-Gd. *Physical Review Materials* **2020**, *4* (2), 024417.

(20) Ishikawa, A.; Hiroto, T.; Tokiwa, K.; Fujii, T.; Tamura, R. Composition-driven spin glass to ferromagnetic transition in the quasicrystal approximant Au-Al-Gd. *Phys. Rev. B: Condens. Matter Mater. Phys.* **2016**, *93* (2), 024416.

(21) Hiroto, T.; Sato, T.; Cao, H.; Hawai, T.; Yokoo, T.; Itoh, S.; Tamura, R. Noncoplanar ferrimagnetism and local crystalline-electric-field anisotropy in the quasicrystal approximant $Au_{70}Si_{17}Tb_{13}$. *J. Phys.: Condens. Matter* **2020**, DOI: 10.1088/1361-648X/ab997d.

(22) Ishikawa, A.; Fujii, T.; Takeuchi, T.; Yamada, T.; Matsushita, Y.; Tamura, R. Antiferromagnetic order is possible in ternary quasicrystal approximants. *Phys. Rev. B: Condens. Matter Mater. Phys.* **2018**, *98* (22), 220403.
(23) Hiroto, T.; Tokiwa, K.; Tamura, R. Sign of canted ferromagnetism in the quasicrystal approximants Au-SM-R (SM = Si, Ge and Sn/R = Tb, Dy and Ho). *J. Phys.: Condens. Matter* **2014**, *26* (21), 216004.
(24) Canfield, P.; Kong, T.; Kaluarachchi, U.; Jo, N. H. Use of frit-disc crucibles for routine and exploratory solution growth of single crystalline samples. *Philos. Mag.* **2016**, *96* (1), 84−92.
(25) Saint, A. *APEX3 software for CCD diffractometers*; Bruker Analytical X-ray Systems Inc.: Madison, WI, 2014.
(26) Petříček, V.; Dušek, M.; Palatinus, L. Crystallographic computing system JANA2006: general features. *Z. Kristallogr. - Cryst. Mater.* **2014**, *229* (5), 345−352.
(27) Palatinus, L.; Chapuis, G. SUPERFLIP−a computer program for the solution of crystal structures by charge flipping in arbitrary dimensions. *J. Appl. Crystallogr.* **2007**, *40* (4), 786−790.
(28) Putz, H.; Brandenburg, K. *DIAMOND-Crystal and molecular structure visualization*; Crystal Impact-GbR, Kreuzherrenstr**2006***10*253227
(29) Momma, K.; Izumi, F. VESTA 3 for three-dimensional visualization of crystal, volumetric and morphology data. *J. Appl. Crystallogr.* **2011**, *44* (6), 1272−1276.
(30) Gebresenbut, G. Quasicrystal approximants in the RE-Au-SM systems (RE= Gd, Tb, Ho, Yb; SM= Si, Ge): syntheses, structures and properties. Acta Universitatis Upsaliensis, 2016.
(31) Okamoto, H.; Massalski, T. The Au-Si (gold-silicon) system. *Bull. Alloy Phase Diagrams* **1983**, *4* (2), 190−198.
(32) Pay Gómez, C. *Order and disorder in the RE-Cd and related systems*. Doctoral Thesis, Stockholms universitet, Stockholm, 2003.
(33) Hiroto, T.; Gebresenbut, G.; Pay Gómez, C.; Muro, Y.; Isobe, M.; Ueda, Y.; Tokiwa, K.; Tamura, R. Ferromagnetism and re-entrant spin-glass transition in quasicrystal approximants Au−SM−Gd (SM= Si, Ge). *J. Phys.: Condens. Matter* **2013**, *25* (42), 426004.
(34) Filho, P. L. C.; Barrozo, P.; Landinez-Tellez, D.; Jardim, R.; Azevedo, W.; Aguiar, J. Structural and magnetic properties of Ln_2CoMnO_6 (Ln = Dy and La) produced by combustion synthesis. *J. Supercond. Novel Magn.* **2013**, *26* (7), 2521−2524.
(35) Tomiyasu, K.; Fukunaga, J.; Suzuki, H. Magnetic short-range order and reentrant-spin-glass-like behavior in $CoCr_2O_4$ and $MnCr_2O_4$ by means of neutron scattering and magnetization measurements. *Phys. Rev. B: Condens. Matter Mater. Phys.* **2004**, *70* (21), 214434.
(36) Mydosh, J. *Spin glasses: an experimental introduction*; Taylor and Francis London: Washington, DC, 1993.

https://dx.doi.org/10.1021/acs.inorgchem.0c01023
Inorg. Chem. 2020, 59, 9152−9162